# A 3D Optical Sensor Using Optical Axis Deviation Method for Rotational Errors

Hau-Wei Lee, Te-Ping Chiu,[1] and Chien-Hung Liu[2]*

Center for Measurement Standards, Industrial Technology Research Institute, HsinChu 300, Taiwan, ROC
[1]Institute of Electro-Optical and Materials Science, National Formosa University, Huwei 632, Taiwan, ROC
[2]Department of Mechanical Engineering, National Chung Hsing University, Taichung 420, Taiwan, ROC

This paper presents a 3D optical sensor system for measuring errors in the motion of a rotating stage or spindle based on optical axis deviation using a precision ball lens. The radial and axial errors can be simultaneously measured during rotation. The 3D sensor consists of two quadrant photodiode detectors (QDs), two laser diodes, and a ball lens mounted on the rotating stage or spindle. Rotational errors cause changes in the optical axis of the ball lens. The resulting deflections of the laser beams are detected by the QDs and their output signals are used to determine errors. The radial and axial rotational errors can be calculated as described by the mathematical model. Experimental results showed that the measuring accuracy was within ±1 μm at a resolution of about 20 nm.

## 1. Introduction

The accuracy of the rotational axes in precision machining has always been a vital factor. To start with, the accuracy of the spindle itself is important, as are the precision and stability of its bearings and their mounting and assembly. Thermal expansion and many other factors are also involved. These all contribute to machining accuracy, and it is important to be able to measure axial, radial, and tilt errors to determine accuracy. At present, most rotational measurements of precision axes are made using non-contact methods. The standard, American National Standards Institute (ANSI)/American Society of Mechanical Engineers (ASME) B89.3.4 "Axes of rotation, methods of specification and testing," was issued in 1985.[1] In 1993, at least three new standards from ASME, British Standards Institution (BSI), and International Organization for Standardization (ISO) 230-7 were published, showing a clear increase in the amount of attention being paid to spindle error analysis. Tlustry[2] was first to use capacitance-based non-contact displacement transducers positioned at 90° to each other in 1959. The two-axis pickup system made it possible for the first time to show the radial error motion of an axis dynamically on a polar plot. In 1967, Bryan *et al.*[3] presented a new approach both in terms of definition and method. They proposed a scheme for measuring spindle error motion with a master ball. Nowadays, the capacitive probe is very widely used in spindle precision testing.[4–6] However, the device has to be set up with a standard test bar in the rotation axis before measurements can be done. Although the capacitance

probe is very precise and has a fast response, the results are susceptible to material surface imperfections, magnetic interference, and other influences.  Much research has been done to reduce measurement errors caused by faulty installation, and many optical methods have been presented to separate the different errors in the rotating axes.  Chu *et al*. used a fiber laser to measure the axial and radial rotational error.[7]  Liu *et al*. developed a measuring system for evaluating the radial and tilt errors in a spindle without using a master sphere or cylinder.[8]  This system uses a rotational fixture with a built-in laser diode mounted on the spindle.  Two measuring devices with two position-sensitive detectors (PSD) are fixed on the machine table to measure the position of the laser spot.  Park *et al*.  proposed a measuring arrangement for five-degrees-of-freedom (DOF) rotational errors, but it was necessary to measure each error separately.[9]  However, individual measurements separated in time can result in the accumulation of errors, such as those from changes in temperature.  Fujimaki *et al*. proposed a radial error measuring device for miniature ultra-high-speed spindles based on auto-collimation using a small steel ball[10] but it could only measure radial error.  Castro used laser interferometry to measure both radial and axial error.[11]  In his method, a lens was used to focus the beam from a Hewlett Packard 5529A laser interferometer onto a high-precision sphere, and both the radial error and axial error were measured separately.  Anandana *et al.* described a method using two laser Doppler vibrometer (LDV) systems to measure the radial motion at two axial locations on a precision cylinder attached to a spindle.[12]  Lee *et al*. attached a concave mirror to a spindle and measured changes in reflection to determine rotational error.[13]  This reduced the mass on the spindle as well as minimizing angular errors during assembly.  However, this setup could not measure both radial and axial error at the same time.  Imperfections in mirror curvature could also cause displacement errors.  Other methods used birefringence heterodyne interferometry, diffraction gratings, and double ball bars to measuring angular errors in rotational stages.[14–17]

In this study, a 3D sensor for the simultaneous measurement of radial and axial error was developed using a ball lens.  The size of the lens used can be as small as 3 mm in diameter, making it useable with very small spindles.  The measurement error caused by imperfect curvature of a ball lens was also analyzed in this study.  In the first part, a description of the 3D sensor is presented, and in the second, an analysis of the 3D optical path and error models are given.  The final part is a discussion of the experimental results.

## 2.    Design of the 3D Sensor

### 2.1    System construction

Figure 1 shows the optical design of the 3D sensor.  It consists of two sets of orthogonal laser diodes, two quadrant photodiode detectors (QDs), and a ball lens.  The lens diameter is 10 mm; the material is BK7, and its sphericity is within 2 μm.  In practical use, the ball lens is fixed on the end of a spindle or in the center of a rotary stage.  In Fig. 1, beam L1 from Laser 1 is focused by the ball lens to give beam L2, and beam L3 from Laser 2 is focused by the ball lens to give beam L4.  The two beams are focused on QD1 and QD2, respectively.  Figure 2 shows the actual experimental setup using two laser diodes and two QDs.  The measurement principle of the optical axis deviation method is shown in Fig. 3.  When there is a deviation shift $\delta_x$ in the ball lens, it causes an offset of light beam L2 resulting in an offset displacement $q_{x1}$ which can be measured by QD1.  If Laser 1 and Laser 2 are set up orthogonally, the following approximate equation can be obtained:
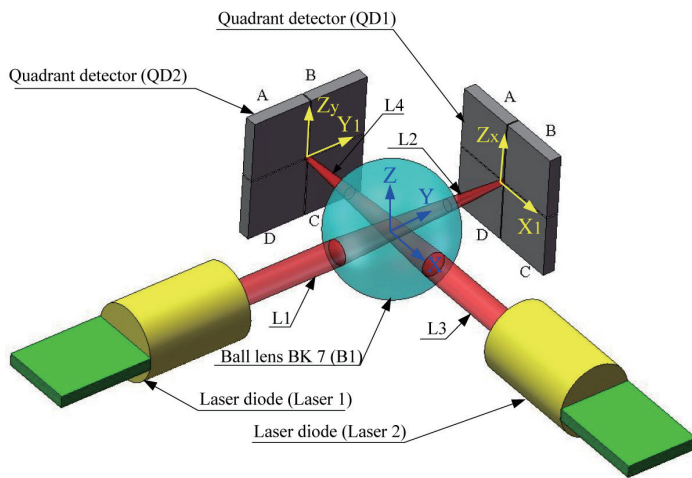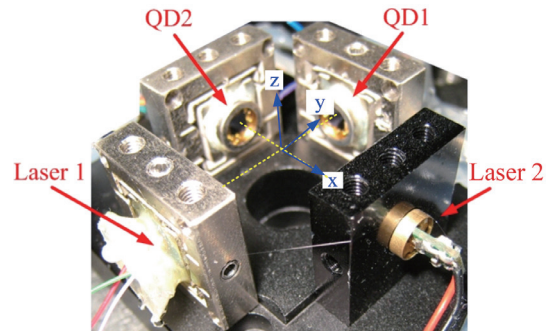
Fig. 1.   (Color online) Arrangement of components for the measurement device.



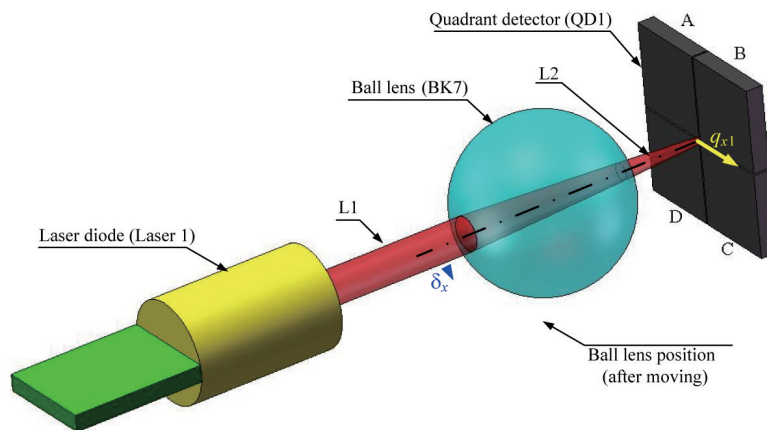Fig. 2.   (Color online) Physical setup.



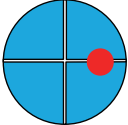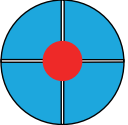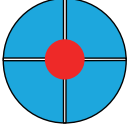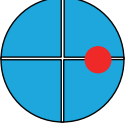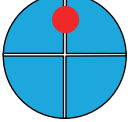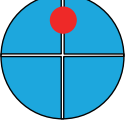Fig. 3.   (Color online) Error measurement: ball lens optical axis deviation.

$$
\begin{bmatrix} \delta_x \\ \delta_y \\ \delta_z \end{bmatrix} = \begin{bmatrix} k_x & 0 & 0 & 0 \\ 0 & 0 & k_y & 0 \\ 0 & \dfrac{k_z}{2} & 0 & \dfrac{k_z}{2} \end{bmatrix} \begin{bmatrix} q_{x1} \\ q_{z1} \\ q_{y1} \\ q_{z2} \end{bmatrix},
\tag{1}
$$

where the displacement of the ball lens is $[\delta_x\ \delta_y\ \delta_z]^{\mathrm{T}}$, which are the radial and axial errors in the axis of rotation.  The displacements of the light spot on the QDs are $(q_{x1}, q_{z1})$ and $(q_{y2}, q_{z2})$.  The terms $k_x$, $k_y$, and $k_z$ are the conversion constants between the QD output voltage and the displacement of the ball lens, which can be obtained from a system calibration.  The sensing directions between displacements of the ball lens in the *x*, *y*, and *z* directions and the change in position of the laser spots on the QDs are all shown in Table 1.

Table 1
(Color online) Direction of ball lens movement and changes of the light spots on the QDs.

| Direction of ball lens movement | QD1 | QD2 |
|---|---|---|
| X | | |
| Y | | |
| Z | | |



## 2.2 Kinematic model analysis

The kinematic model can be represented as a vector as shown in Fig. 4. Assume the angle between laser beams L1 and L2 is $\theta_{in2}$. The original coordinate system of the ball lens is represented by {L}, and {L′} is a new coordinate for the center deviation of the ball lens. The coordinate systems of {Q1} and {Q2} are represented as the coordinate system of QD1 and QD2. Vector $\vec{s} = [\delta_x \ \delta_y \ \delta_z]^T$ represents the translation vector between coordinate systems {L} and {L′}. The positional vectors of the laser spots on QD1 and QD2 are represented as $\vec{q_1} = [q_{1x} \ 0 \ q_{1z}]$ and $\vec{q_2} = [0 \ q_{2y} \ q_{2z}]$, respectively. The distance vectors from the center of {L} to {Q1} and {Q2} are $\vec{d}_{L1}$ and $\vec{d}_{L2}$, respectively. The terms $\vec{u}_{L1}$ and $\vec{u}_{L2}$ are units of vectors $\vec{d}_{L1}$ and $\vec{d}_{L2}$. Figure 5 shows the analysis of the laser beam L1 system. As seen in Fig. 4, for the laser beam L2 system, displacement of the ball lens denoted by $\vec{s'} = [\delta_x' \ \delta_y' \ \delta_z']^T$ can be computed using the following equations:

$$\vec{s'} = \boldsymbol{R}_{in}^{-1} \, \vec{s}, \tag{2}$$

$$\boldsymbol{R}_{in} = \begin{bmatrix} \cos\theta_{in2} & -\sin\theta_{in2} & 0 \\ \sin\theta_{in2} & \cos\theta_{in2} & 0 \\ 0 & 0 & 1 \end{bmatrix}, \tag{3}$$

making the distance from the ball lens center to QD1 to be $\vec{v}_{q1} = [0 \ d_{qy1} \ 0]^T$. As can be seen in Fig. 5, it has been established that the distance vector from the center to the incident light on the ball lens surface is $\vec{v}_{R1} = \left[ -\delta_x \ \ -\sqrt{R_1^2 - \delta_x^2 - \delta_z^2} \ \ -\delta_z \right]^T$ and the distance vector from the center to the penetrating light on the ball lens surface is $\vec{v}_{R2} = \left[ d_{outx} \ \ \sqrt{R_2^2 - d_{outx}^2 - d_{outz}^2} \ \ d_{outz} \right]^T$, where $R_1$ and $R_2$ are the radii of the incident light and the penetrating light on the ball lens surface to its center. The terms $\vec{v}_{R1}$ and $\vec{v}_{R2}$ can be expressed as normal vectors of incident and penetrating light, respectively. According to Snell's Law:
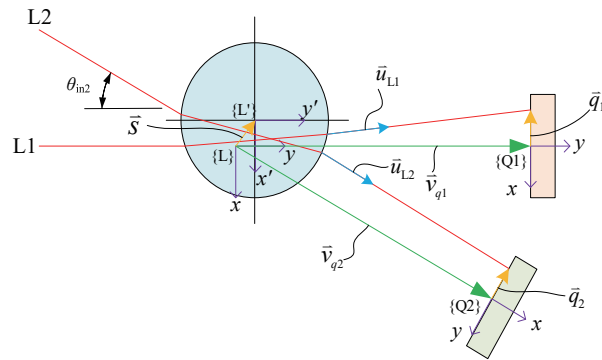
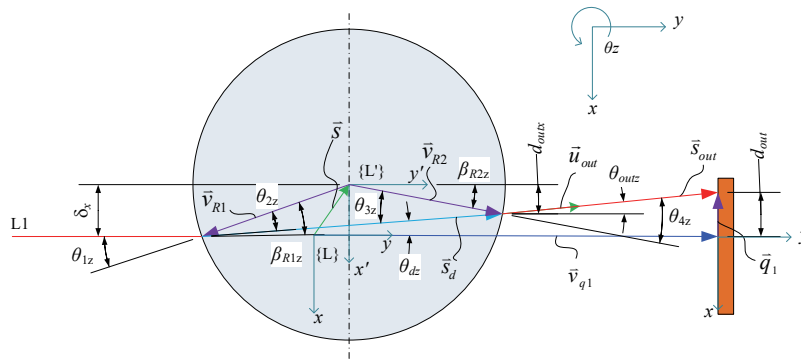Fig. 4.   (Color online) Kinematic model of the optical system.



Fig. 5.   (Color online) Kinematic analysis of optical axis deviation.

$$\begin{cases} n_1 \sin \theta_{1x} = n_2 \sin \theta_{2x}, \\ n_1 \sin \theta_{1z} = n_2 \sin \theta_{2z}, \end{cases} \tag{4}$$

$$\therefore \begin{cases} \theta_{1x} = \beta_{R1x} = \sin^{-1} \dfrac{\delta_z}{|R_1|}, \\ \theta_{1z} = \beta_{R1z} = -\sin^{-1} \dfrac{\delta_x}{|R_1|}, \end{cases} \tag{5}$$

$$\therefore \begin{cases} \theta_{dx} = \beta_{R1x} - \theta_{2x} = \sin^{-1} \dfrac{\delta_z}{|R_1|} - \sin^{-1} \left( \dfrac{n_1}{n_2} \dfrac{\delta_z}{|R_1|} \right), \\ \theta_{dz} = \beta_{R1z} - \theta_{2z} = -\sin^{-1} \dfrac{\delta_x}{|R_1|} + \sin^{-1} \left( \dfrac{n_1}{n_2} \dfrac{\delta_x}{|R_1|} \right), \end{cases} \tag{6}$$

where $\theta_1$ is the angle between the incident light and its normal vector, $\theta_2$ is the angle between the light travel direction in the ball lens and the normal vector of the incident light, $\beta_{R1x}$ and $\beta_{R1z}$ are the angles between the normal vector of the incident light and $x$-axis and $z$-axis, $\theta_{dx}$ and $\theta_{dz}$ are the angles between the displacement vector $\vec{s}_d$ for the light traveling in the ball lens and $x$-axis as well as in the $z$-axis, and $\vec{s}_d$ can be computed by

$$
\vec{s}_d = \begin{bmatrix} 1 & 0 & 0 \\ 0 & \cos\theta_{dx} & -\sin\theta_{dx} \\ 0 & \sin\theta_{dx} & \cos\theta_{dx} \end{bmatrix} \begin{bmatrix} \cos\theta_{dz} & -\sin\theta_{dz} & 0 \\ \sin\theta_{dz} & \cos\theta_{dz} & 0 \\ 0 & 0 & 1 \end{bmatrix} \begin{bmatrix} 0 \\ l_1 \\ 0 \end{bmatrix}, \tag{7}
$$

where $l_1$ is the distance the beam travels through the lens, which is unknown. Thus, the distance vector from the sphere center to the penetrating light on the ball lens surface can be determined by:

$$
\vec{v}_{R2} = \vec{v}_{R1} + \vec{s}_d. \tag{8}
$$

After developing Eq. (8), the following is obtained:

$$
\begin{cases} d_{outx} + l_1 \sin\theta_{dz} + \delta_x = 0, \\ d_{outz} - l_1 \cos\theta_{dz} \sin\theta_{dx} + \delta_z = 0, \\ \sqrt{R_1^2 - \delta_x^2 - \delta_z^2} - \sqrt{R_2^2 - d_{outx}^2 - d_{outz}^2} - l_1 \cos\theta_{dx} \cos\theta_{dz} = 0. \end{cases} \tag{9}
$$

In Eq. (9), the unknowns to be determined are $l_1$, $d_{outx}$, and $d_{outz}$. These can be determined from Eq. (9) after $\theta_{dx}$ and $\theta_{dz}$ have been determined as follows. When the laser beam is off the ball lens, the angle of departure is

$$
\begin{cases} \theta_{outx} = -\beta_{R2x} + \theta_{4x} = \sin^{-1}\dfrac{d_{outz}}{|R_2|} + \sin^{-1}\left(\dfrac{n_2}{n_1}\sin\theta_{3x}\right), \\ \theta_{outz} = -\beta_{R2z} + \theta_{4z} = -\sin^{-1}\dfrac{d_{outx}}{|R_2|} + \sin^{-1}\left(\dfrac{n_2}{n_1}\sin\theta_{3z}\right), \end{cases} \tag{10}
$$

$$
\begin{cases} \theta_{3x} = \beta_{R2x} + \theta_{dx} = -\sin^{-1}\dfrac{d_{outz}}{|R_2|} + \theta_{dx}, \\ \theta_{3z} = \beta_{R2z} + \theta_{dz} = \sin^{-1}\dfrac{d_{outx}}{|R_2|} + \theta_{dz}, \end{cases} \tag{11}
$$

where $\theta_3$ is the angle between the penetrating light beam and its normal vector, $\theta_4$ is the angle between the transmitted light that has left the ball lens and its normal vector, and $\beta_{R2x}$ and $\beta_{R2z}$ are the angles between the normal vector of transmitted light and the $x$-axis and $z$-axis. The focusing direction of the beam after it has passed through the ball lens can be represented by a unit vector:

$$
\vec{u}_{out} = \begin{bmatrix} 1 & 0 & 0 \\ 0 & \cos\theta_{outx} & -\sin\theta_{outx} \\ 0 & \sin\theta_{outx} & \cos\theta_{outx} \end{bmatrix} \begin{bmatrix} \cos\theta_{outz} & -\sin\theta_{outz} & 0 \\ \sin\theta_{outz} & \cos\theta_{outz} & 0 \\ 0 & 0 & 1 \end{bmatrix} \begin{bmatrix} 0 \\ 1 \\ 0 \end{bmatrix} = \begin{bmatrix} -\sin\theta_{outz} \\ \cos\theta_{outx}\cos\theta_{outz} \\ \sin\theta_{outx}\cos\theta_{outz} \end{bmatrix}. \tag{12}
$$

From Fig. 5 it can be deduced that the displacement vector of the light spot projected on QD1 is

$$
\vec{q}_1 = \vec{s} + \vec{v}_{R2} + \vec{s}_{out} - \vec{v}_{q1} = \vec{s} + \vec{v}_{R2} + l_2\vec{u}_{out} - \vec{v}_{q1}, \tag{13}
$$

where $\vec{s}_{out}$ is the displacement vector of the focused light, which can be substituted by $l_2\vec{u}_{out}$, and $l_2$ is the vector length of $\vec{s}_{out}$. After expanding Eq. (13), it can be seen that:

$$\begin{cases} q_{1x} - \delta_x - d_{\text{out}x} + l_2 \sin\theta_{\text{out}z} = 0, \\ q_{1z} - \delta_z - d_{\text{out}z} - l_2 \sin\theta_{\text{out}x}\cos\theta_{\text{out}z} = 0, \\ d_{qy1} - \delta_y - \sqrt{R_2^2 - d_{\text{out}x}^2 - d_{\text{out}z}^2} - l_2 \cos\theta_{\text{out}x}\cos\theta_{\text{out}z} = 0. \end{cases} \tag{14}$$

The solution to the above is

$$\begin{cases} q_{1x} = d_{\text{out}x} + \delta_x + \dfrac{\delta_y + \sqrt{R_2^2 - d_{\text{out}x}^2 - d_{\text{out}z}^2} - d_{qy1}}{\cos\theta_{\text{out}x}} \tan\theta_{\text{out}z}, \\ q_{1z} = d_{\text{out}z} + \delta_z - \left(\delta_y + \sqrt{R_2^2 - d_{\text{out}x}^2 - d_{\text{out}z}^2} - d_{qy1}\right)\tan\theta_{\text{out}x}. \end{cases} \tag{15}$$

## 2.3    Model simplification

When the displacement of the ball lens is small, paraxial optics can be used to simplify the measurement model.  Simplified Eqs. (6) and (7) are as follows:

$$\begin{cases} \theta_{\text{d}x} \cong \dfrac{n_2 - n_1}{n_2 |R_1|}\delta_z, \\ \theta_{\text{d}z} \cong -\dfrac{n_2 + n_1}{n_2 |R_1|}\delta_x, \end{cases} \tag{16}$$

$$\vec{s}_{\text{d}} \cong \begin{bmatrix} 1 & 0 & 0 \\ 0 & 1 & -\theta_{\text{d}x} \\ 0 & \theta_{\text{d}x} & 1 \end{bmatrix} \begin{bmatrix} 1 & -\theta_{\text{d}z} & 0 \\ \theta_{\text{d}z} & 1 & 0 \\ 0 & 0 & 1 \end{bmatrix} \begin{bmatrix} 0 \\ l_1 \\ 0 \end{bmatrix}. \tag{17}$$

Under paraxial conditions, the distance the light beam travels in passing through the ball lens is close to the diameter of the ball lens:

$$l_1 \cong |R_1| + |R_2|. \tag{18}$$

Substituting Eqs. (16) to (18) into Eq. (9) and linearizing, $d_{\text{out}x}$ and $d_{\text{out}z}$ can be simply computed by:

$$\begin{cases} d_{\text{out}x} \cong \left[\dfrac{(|R_1| + |R_2|)(n_2 - n_1)}{n_2 |R_1|} - 1\right]\delta_x, \\ d_{\text{out}z} \cong \left[\dfrac{(|R_1| + |R_2|)(n_2 - n_1)}{n_2 |R_1|} - 1\right]\delta_z. \end{cases} \tag{19}$$

Similarly, Eqs. (10) and (12) can be simplified as:

$$\begin{cases} \theta_{\text{out}x} \cong \dfrac{(n_2 - n_1)(|R_1| + |R_2|)}{n_2 |R_1||R_2|}\delta_z, \\ \theta_{\text{out}z} \cong -\dfrac{(n_2 - n_1)(|R_1| + |R_2|)}{n_2 |R_1||R_2|}\delta_x, \end{cases} \tag{20}$$

$$\vec{u}_{\text{out}} \cong \begin{bmatrix} -\theta_{\text{outz}} & 1 & \theta_{\text{outx}} \end{bmatrix}^{\text{T}}. \tag{21}$$

After simplification of Eq. (14), we have:

$$\begin{cases} q_{1x} - \delta_x - d_{\text{outx}} + l_2\theta_{\text{outz}} = 0, \\ q_{1z} - \delta_z - d_{\text{outz}} - l_2\theta_{\text{outx}} = 0, \\ d_{qy1} - \delta_y - \sqrt{R_2^2 - d_{\text{outx}}^2 - d_{\text{outz}}^2} - l_2 = 0. \end{cases} \tag{22}$$

Finally, by substituting Eqs. (19) and (20) into Eq. (22), the measurement equation can be determined:

$$\begin{cases} q_{1x} = \dfrac{(n_2-n_1)(|R_1|+|R_2|)(d_{qy1}+|R_2|-\delta_y-\mu)}{n_2|R_1||R_2|}\delta_x, \\[2mm] q_{1z} = \dfrac{(n_2-n_1)(|R_1|+|R_2|)(d_{qy1}+|R_2|-\delta_y-\mu)}{n_2|R_1||R_2|}\delta_z, \end{cases} \tag{23}$$

$$\mu = \sqrt{R_2^2 - \left[\frac{\big(n_2|R_2|-n_1|R_1|+n_1|R_2|\big)\delta_x}{n_2|R_1|}\right]^2 - \left[\frac{\big(n_2|R_2|-n_1|R_1|+n_1|R_2|\big)\delta_z}{n_2|R_1|}\right]^2}. \tag{24}$$

For QD2, the measurement equation can be rewritten as:

$$\begin{cases} q_{2y} = \dfrac{(n_2-n_1)(|R_3|+|R_4|)(d_{qx2}+|R_4|-\delta_y'-\mu')}{n_2|R_3||R_4|}\delta_x', \\[2mm] q_{2z} = \dfrac{(n_2-n_1)(|R_3|+|R_4|)(d_{qx2}+|R_4|-\delta_y'-\mu')}{n_2|R_3||R_4|}\delta_z', \end{cases} \tag{25}$$

$$\mu' = \sqrt{R_4^2 - \left[\frac{\big(n_2|R_4|-n_1|R_3|+n_1|R_4|\big)\delta_x'}{n_2|R_3|}\right]^2 - \left[\frac{\big(n_2|R_4|-n_1|R_3|+n_1|R_4|\big)\delta_z'}{n_2|R_3|}\right]^2}, \tag{26}$$

where $R_3$ and $R_4$ are the radii of L2 incident light and penetrating light on the surface of the ball lens to the sphere center. Since the mounting angle between QD2 and QD1 used here is 90°, Eq. (2) can be simplified to:

$$\begin{bmatrix} \delta_x' \\ \delta_y' \\ \delta_z' \end{bmatrix} = \begin{bmatrix} -\delta_y \\ \delta_x \\ \delta_z \end{bmatrix}. \tag{27}$$

Using Eqs. (23) and (25), the constants of proportionality $k_x$, $k_y$, and $k_z$ in Eq. (1) can be obtained.

## 2.4    Analysis of the sphericity error of the ball lens

Because a ball lens in never a perfect sphere, the equations for the actual distance from the spherical center where the laser beam hits the surface and where it leaves the sphere should be amended as follows:

$$\begin{cases} R'_1 = R_1 + \sigma_{R1}, \\ R'_2 = R_2 + \sigma_{R2}, \end{cases} \tag{28}$$

where $\sigma_{R1}$ and $\sigma_{R2}$ are the radius errors of the ball lens. Simulation was used here to estimate the effect of the radius error on the measured results. Because L1 and L2 have the same optical properties, only one was analyzed. We assumed both $R_1$ and $R_2$ were 5 mm; the refractive index of air is $n_1 = 1$. The distance from QD1 to the center of the ball lens is 20 mm. It was also assumed that when the ball lens was rotating, the deviation from its rotational axis $\delta_z$ was only 0.1 mm, and the ball lens radius error was 0.01 mm. The simulation results are shown in Fig. 6. As can be seen, the maximum measurement error was 0.1 μm with a maximum ball radius error of 0.01 mm.

However, the ball lens displacement $\delta_y$ in the L1 measurement path might cause coupling displacement in the other sensing directions. A simulated result is shown in Fig. 7. In this simulation, $\delta_y$ was given within ±0.1 mm, $\delta_z$ was 0.1 mm, and $\delta_x$ was 0.0 mm. The simulation results showed that, when the ball lens moved 0.1 mm along the light optical axis, the measurement error was within ±0.7 μm.
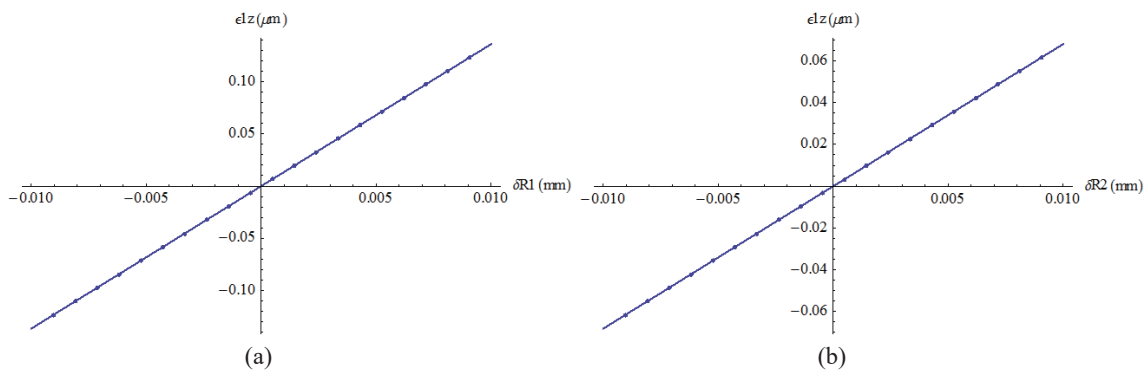


Fig. 6.    (Color online) Measurement error caused by imperfections in sphericity of the ball lens: (a) $\sigma_{R1}$ within ±0.1 mm and (b) $\sigma_{R2}$ within ±0.1 mm.
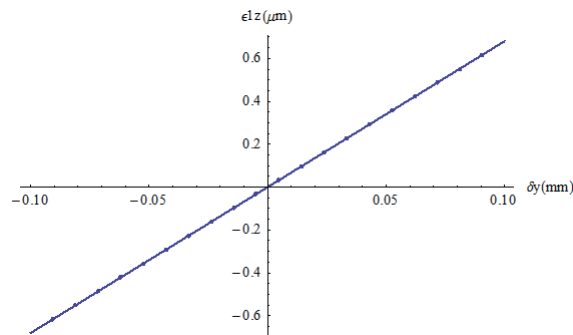


Fig. 7.    (Color online) The measurement error in the $z$ direction caused by $\delta_y$.

## 3.    Experimental Results

### 3.1    System calibration

An *X*-, *Y*- and *Z*-axis nanometer stage was used to calibration the system.  The ball lens was fixed on the stage and moved in steps of 20 nm to test resolution.  The recorded displacement was compared with the output voltage of QD to determine a displacement-to-voltage conversion constant.  Figure 8(a) shows the resolution test (after conversion to displacement) of the sensor.  The resolution was about 20 nm.  The stage was then moved to ±50 µm with stepwise inputs of 5 µm to carry out an accuracy test.  Figures 8(b) and 8(c) show that the radial and axial accuracies were within ±1.0 µm, respectively.

### 3.2    Static rotational test of a direct drive (DD) motor stage

The experimental setup is shown in Fig. 9.  The static rotational tests for radial and axial error measurements were made with the DD motor operating in the positioning mode.  The ball lens was fixed to the stage and rotated by the DD motor in 10° steps.  The *X*-, *Y*-, and *Z*-directional rotational errors were measured, as shown in Fig. 10.  The error deviations in the *X*-, *Y*-, and *Z*-directions were 20, 32, and 3.5 µm without eccentricity compensation.  The standard deviation of the sensor was less than 0.015 µm, as shown in Fig. 11, which reveals a sufficiently high sensor precision.
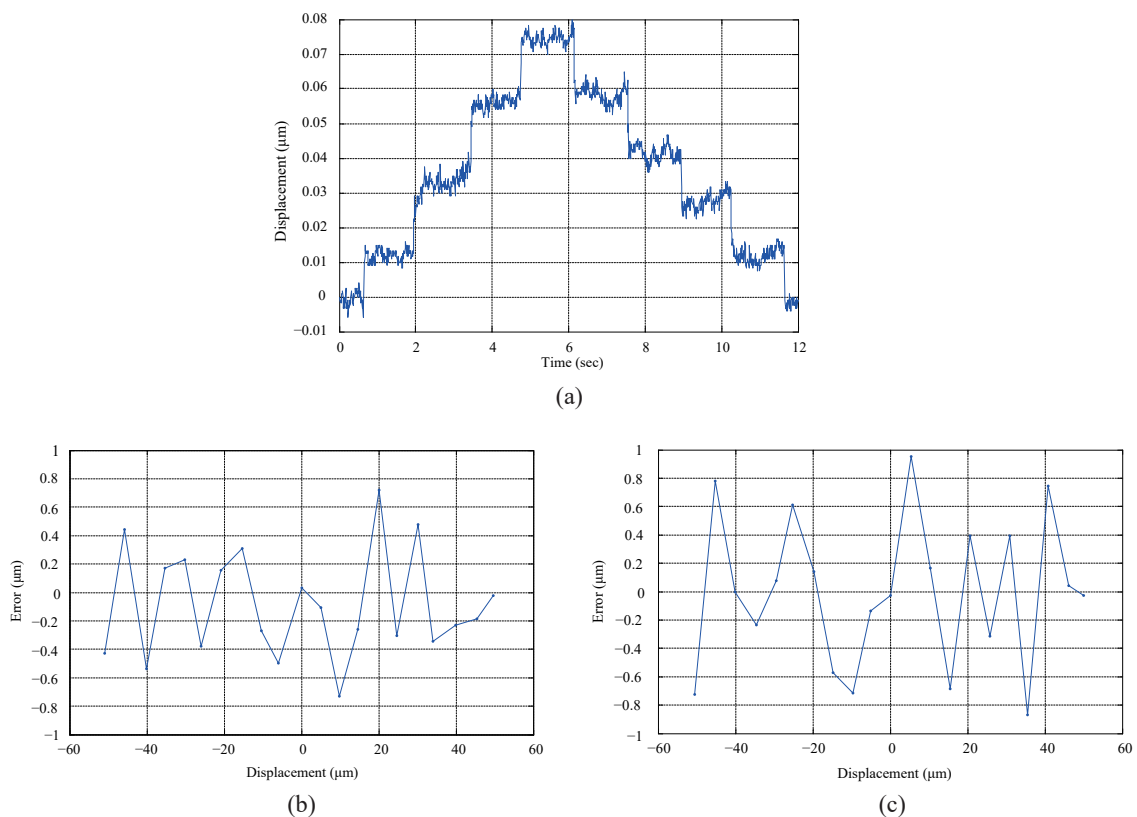


(a)



(b)



(c)

Fig. 8.    (Color online) 3D sensor calibration test: (a) resolution; (b) radial accuracy; and (c) axial accuracy.
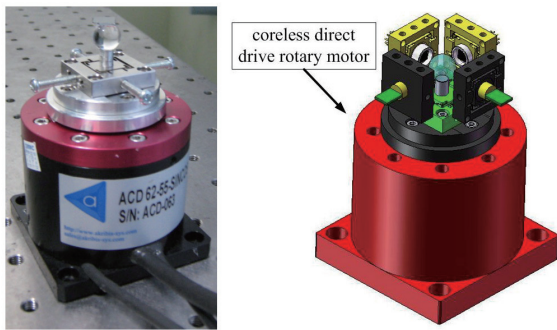
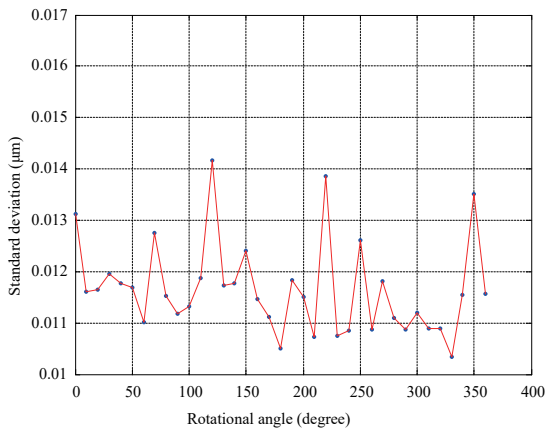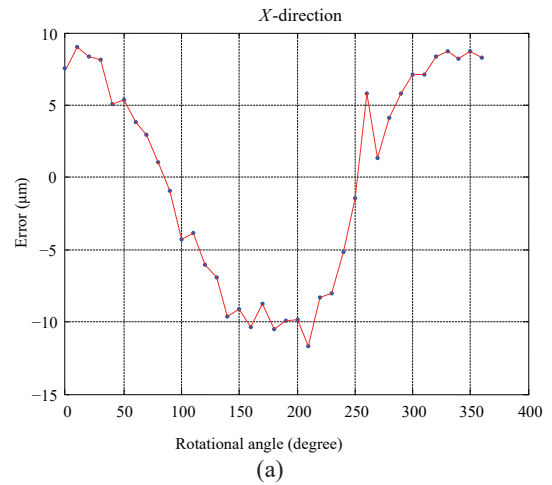Fig. 9.   (Color online) Experimental setup using the 3D sensor.



Fig. 11. (Color online) Standard deviation of the sensor.
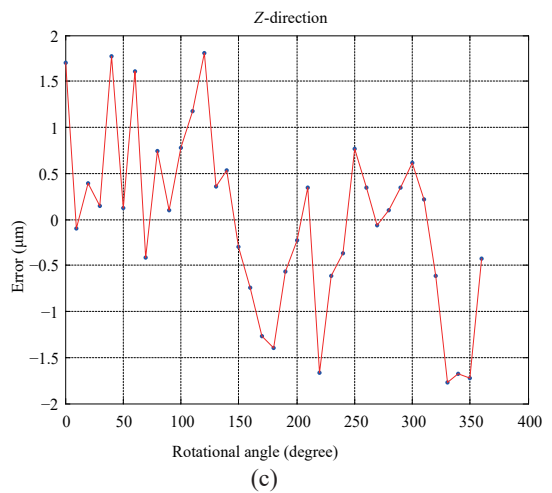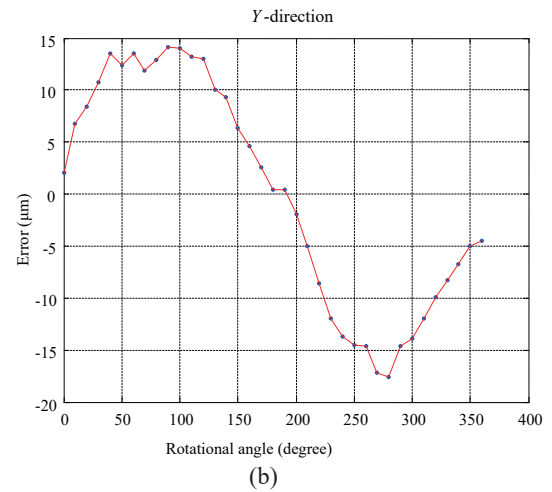


(a)



(b)



(c)

Fig. 10. (Color online) Static error tests of a DD motor actuated rotating stage: (a) *X*-direction; (b) *Y*-direction; and (c) *Z*-direction.

### 3.3    Dynamic rotational tests using the DD motor stage

Dynamic rotational tests were carried out at 12, 72, and 120 rpm. The experimental results of radial error measurements are shown in Figs. 12–14 and the results are summarized in Table 2. At 12 rpm, the synchronous and asynchronous errors were 8.82 and 12.13 µm. When the rotational speed was increased to 120 rpm, the synchronous and asynchronous errors were 8.64 and 13.19 µm, respectively. The rotation speeds of 12 and 120 rpm are not very high, and the results showed that the dominant errors were those induced by the ball bearings. The proposed sensor was shown to be flexible and versatile and perfectly suitable for measuring rotational errors in both the stage and the small spindle. The diameter of the ball lens used can be selected to suit the purpose in each case.
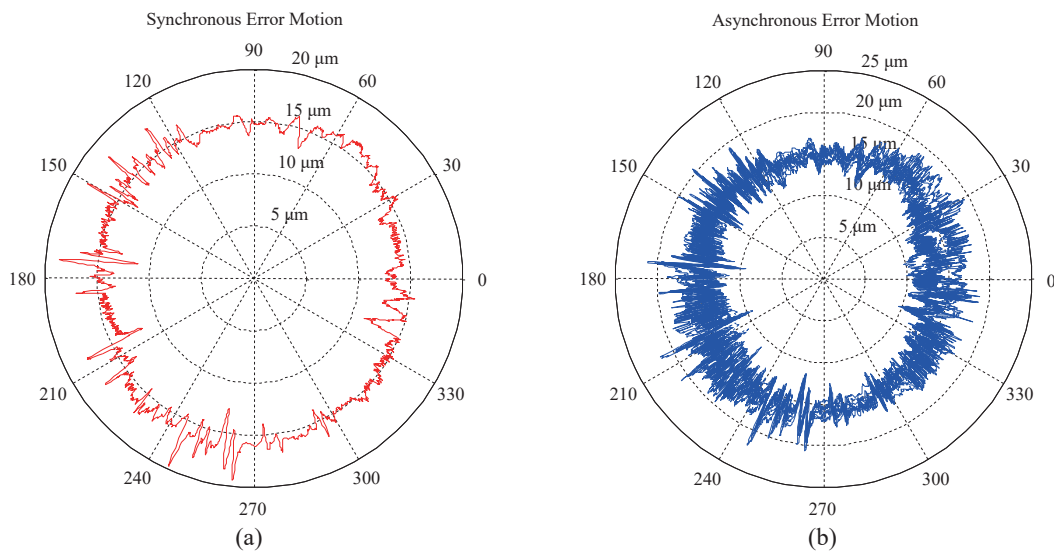


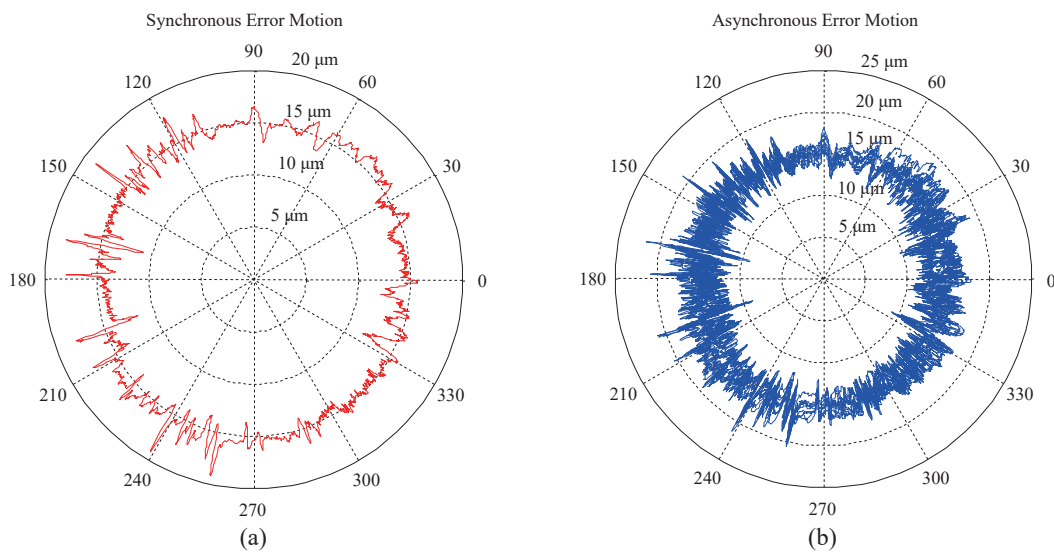Fig. 12.   (Color online) Radial error measurement at 12 rpm.



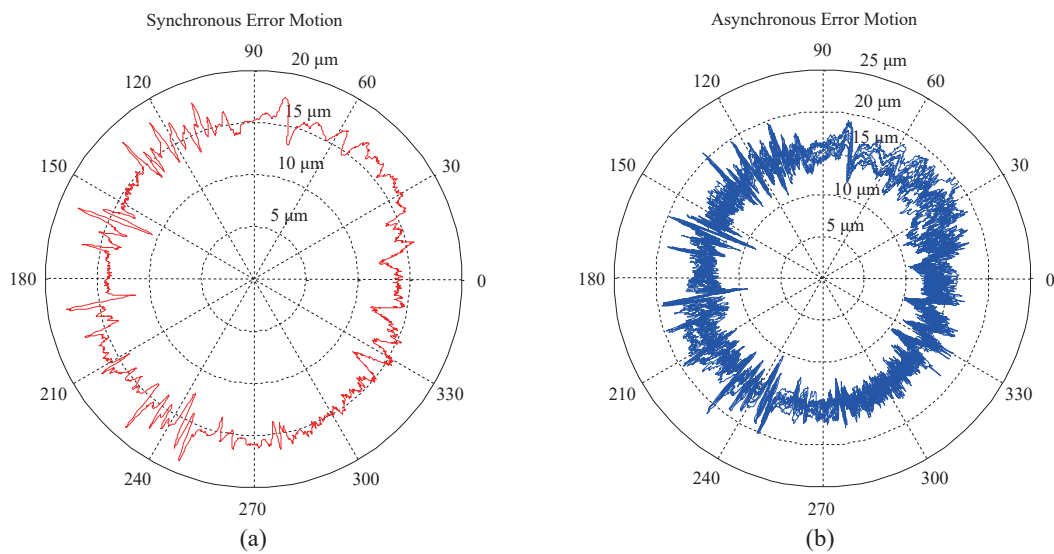Fig. 13.   (Color online) Radial error measurement at 72 rpm.

Fig. 14.  (Color online) Radial error measurement at 120 rpm.

Table 2
Dynamic error measurement results.

| Rotational speed (rpm) | Synchronous error motion (μm) | Asynchronous error motion (μm) |
|---|---|---|
| 12 | 8.82 | 12.13 |
| 72 | 8.31 | 12.84 |
| 120 | 8.64 | 13.19 |

## 4.    Conclusion

This paper describes the design of a flexible and accurate method for measuring the accuracy of rotation on a meso- and micro-scale.  Tests of this 3D optical method for the measurement of radial and axial rotational errors using a precision ball lens have been shown to be precise and reproducible.  Kinematic analysis was used to characterize a measuring and error analysis model. The results showed that the influence of the sphericity of the ball lens was estimated to be small. This 3D device is not expensive, has high precision, and is flexible and easy to set up as a rotation measuring system.

## Acknowledgements

# References

1   ASME 1986 Axes of Rotation, Methods for Specifying and Testing ANSI/ASME B89.3.4–1985 (ASME, New York, 1986).
2   J. Tlustry: Microtechnic **13** (1959) 162.
3   J. B. Bryan, R. W. Clouser, and E. Holland: Am. Machinist. **4** (1967) 149.
4   E. Marsh and R. Grejda: Precis. Eng. **24** (2000) 50.
5   R. Grejda, E. Marsh, and R. Vallance: Precis. Eng. **29** (2005) 113.
6   S. D. Ashok and G. L. Samuel: Int. J. Adv. Manuf. Technol. **59** (2012) 445.
7   Y. Chu, F. Xu, T. Ding, and S. Chen: Opt. Eng. **45** (2006) 084403.
8   C. H. Liu, W. Y. Jywe, and H. W. Lee: Meas. Sci. Technol. **15** (2004) 1733.
9   S.-R. Park, T.-K. Hoang, and S.-H. Yang: J. Mech. Sci. Technol. **24** (2010) 175.
10  K. Fujimaki and K. Mitsui: Int. J. Mach. Tools Manuf. **47** (2007) 1677.
11  H. F. F. Castro: Measurement **41** (2008) 526.
12  K. P. Anandana, A. S. Tulsiana, A. Donmezb, and O. B. Ozdoganlara: Precis. Eng. **36** (2012) 104.
13  H.-W. Lee, C.-H. Liu, and W.-H. Lin: J. Chin. Soc. Mech. Eng. **35** (2014) 149.
14  L.-Y Chen, J.-Y Lee, H.-S Chang, and Y. Yang: Smart Sci. **3** (2015) 188.
15  G.-A Jiang and J.-Y Lee: Smart Sci. **2** (2014) 139.
16  C.-H Liu, W.-Y Jywe, L.-H Shyu, and C.-J Chen: Precis. Eng. **29** (2005) 440.
17  C.-K Chen, C.-H Liu, and C.-H Cheng: Smart Sci. **1** (2013) 1.
18  K.-I. Lee, D.-M. Lee, and S.-H. Yang: Int. J. Adv. Manuf. Technol. **62** (2012) 741.